Geophys. J. Int. (2007) **170,** 635–648 doi: 10.1111/j.1365-246X.2006.03279.x

Seismic imaging of the laterally varying D″ region beneath the Cocos Plate

Michael S. Thorne,[1,*] Thorne Lay,[2] Edward J. Garnero,[1] Gunnar Jahnke[3,†] and Heiner Igel[3]

[1]*Department of Geological Sciences, Arizona State University, Tempe, AZ* 85287-1404, *USA. E-mail: mthorne@gi.alaska.edu*
[2]*Department of Earth and Planetary Sciences, University of California Santa Cruz, Santa Cruz, CA* 95064, *USA*
[3]*Department of Earth and Environmental Sciences, Ludwig Maximilians Universität, Theresienstrasse* 41, 80333 *Munich, Germany*

Accepted 2006 November 3. Received 2006 November 2; in original form 2005 September 13

SUMMARY

We use an axisymmetric, spherical Earth finite difference algorithm to model *SH*-wave propagation through cross-sections of laterally varying lower mantle models beneath the Cocos Plate derived from recent data analyses. Synthetic seismograms with dominant periods as short as 4 s are computed for several models: (1) a D″ reflector 264 km above the core–mantle boundary with laterally varying *S*-wave velocity increases of 0.9–2.6 per cent, based on localized structures from a 1-D double-array stacking method; (2) an undulating D″ reflector with large topography and uniform velocity increase obtained using a 3-D migration method and (3) cross-sections through the 3-D mantle *S*-wave velocity tomography model TXBW. We apply double-array stacking to assess model predictions of data. Of the models explored, the *S*-wave tomography model TXBW displays the best overall agreement with data. The undulating reflector produces a double *Scd* arrival that may be useful in future studies for distinguishing between D″ volumetric heterogeneity and D″ discontinuity topography. Synthetics for the laterally varying models show waveform variability not observed in 1-D model predictions. It is challenging to predict 3-D structure based on localized 1-D models when lateral structural variations are on the order of a few wavelengths of the energy used, particularly for the grazing geometry of our data. Iterative approaches of computing synthetic seismograms and adjusting model characteristics by considering path integral effects are necessary to accurately model fine-scale D″ structure.

Key words: core-mantle boundary, global seismology, lateral heterogeneity, mantle discontinuities, seismic wave propagation, synthetic seismograms.

1 INTRODUCTION

1.1 Lower-mantle discontinuities

Ever since the designation of the D″ region (Bullen 1949), consisting of inhomogeneous velocity structure in the lowermost 200–300 km of the mantle, researchers have sought to characterize the detailed nature of this boundary layer. The mechanisms responsible for D″ heterogeneity, manifested in strong arrival time and amplitude fluctuations of seismic phases sampling the region, are still poorly constrained. It is important to characterize the D″ region because its role as a major internal thermal boundary layer of Earth affects many disciplines, including mineral physics, global geodynamics, geochemistry and geomagnetism (see Lay *et al.* 2004a, for a review).

The existence of a D″ velocity discontinuity has been revealed by several seismological techniques. The discontinuity is most commonly inferred based on observation of a traveltime triplication in *S* and/or *P* waves bottoming in the lowermost mantle (see Wysession *et al.* 1998, for a review). Modelling of the triplication waveforms has characterized the D″ discontinuity as being a rapid *P*- and/or *S*-wave velocity (V_P and/or V_S) increase (∼0.5–3.0 per cent for V_P and ∼0.9–3.0 per cent for V_S) ranging in height from 150 to 350 km above the core–mantle boundary (CMB) with an average height of 250 km.

In general, past studies have not established whether a D″ *P*-wave velocity discontinuity is ubiquitous or intermittent (see Wysession *et al.* 1998, for a discussion). In contrast, *S*-wave reflections from a D″ discontinuity are more common, and we will focus on *S* observations. There are three regions of the deep mantle where the existence of a D″ *S*-wave velocity discontinuity is particularly

*Now at: Arctic Region Supercomputing Center, University of Alaska, Fairbanks, AK 99775-6020, USA.
†Now at: Federal Institute of Geosciences and Natural Resources, Stilleweg 2, 30655 Hanover, Germany.

well supported by *S*-wave observations: beneath Siberia (e.g. Lay & Helmberger 1983; Weber & Davis 1990; Gaherty & Lay 1992; Weber 1993; Valenzuela & Wysession 1998; Thomas *et al.* 2004b), beneath Alaska (e.g. Lay & Helmberger 1983; Young & Lay 1990; Lay & Young 1991; Kendall & Shearer 1994; Matzel *et al.* 1996; Garnero & Lay 1997; Lay *et al.* 1997), and beneath Central America (e.g. Lay & Helmberger 1983; Zhang & Lay 1984; Kendall & Shearer 1994; Kendall & Nangini 1996; Ding & Helmberger 1997; Ni *et al.* 2000; Garnero & Lay 2003; Lay *et al.* 2004b; Thomas *et al.* 2004a; Hutko *et al.* 2006; Sun *et al.* 2006). Additional studies have shown evidence for a D″ shear velocity discontinuity beneath the Central Pacific (Garnero *et al.* 1993; Avants *et al.* 2006; Lay *et al.* 2006). This has motivated speculation that the feature is global (e.g. Sidorin *et al.* 1999). Nevertheless, further probing of the deep mantle, especially under the Southern Pacific and Atlantic Ocean regions, is needed before the lateral extent of the feature can be ascertained.

Some locations in the deep mantle where seismic observations do not show evidence for a shear wave discontinuity are adjacent to regions where observations do indicate the presence of a discontinuity. Explanations of why the discontinuity may appear or disappear over small spatial scales (e.g. <100 km, see Lay *et al.* 2004b) are still debated. Large topographic relief on the discontinuity and/or rapid 3-D velocity variations beneath the discontinuity have been invoked as possible explanations (e.g. Kendall & Nangini 1996; Thomas *et al.* 2004a).

1.2 *S*-wave triplication behaviour

We restrict our attention to *S* waves observed on transverse component (*SH*) recordings at epicentral distances ranging from roughly 70° to 85°. Fig. 1 shows synthetic *SH* displacement seismograms computed for the PREM (Dziewonski & Anderson 1981) shear velocity structure (dotted lines) and for a D″ discontinuity model with a 1.3 per cent V_S increase (relative to PREM) 264 km above the CMB (solid lines). Neither model has crustal layers, as discussed below.

Synthetics for the discontinuity model exhibit a traveltime triplication with extra arrivals between *S* and the core-reflection, *ScS*. We use the nomenclature of Lay & Helmberger (1983) to describe the triplication phases labelled in Fig 1. The direct *S* wave turning above the discontinuity is termed *Sab*, whereas the *S*-wave energy turning below the discontinuity is termed *Scd*. *Sbc* denotes arrivals reflecting off the discontinuity. The post-critical *Sbc* arrival is progressively phase shifted as distance increases, producing a small negative overshoot of the combined *Scd* + *Sbc* arrival. In Fig. 1 distinct *Scd* and *Sbc* arrivals are only discernible at larger distances; the *Scd* and *Sbc* arrivals are generally not separately distinguishable in broad-band data. Hence, we refer to the combined (*Scd* + *Sbc*) arrival as *SdS*. Most studies reference *SdS* traveltimes and amplitudes to *ScS* (labelled in Fig. 1). Because the synthetics shown in Fig. 1 were created for a 500 km deep source, the seismic phase *s400S*, an underside reflection from the 400 km discontinuity above the source, is also present. The amplitude of *s400S* is usually too low to be observed in broad-band data without stacking records (e.g. Flanagan & Shearer 1998).

Fig. 2 shows the ray path geometry of the seismic phases in Fig. 1 for an epicentral distance of 75° computed for the discontinuity model used to create the synthetic seismograms in Fig. 1. Also shown in Fig. 2 is the *SH*-velocity wavefield at one instance in time through a cross-section of the Earth computed with the finite difference method discussed below. The relationship between

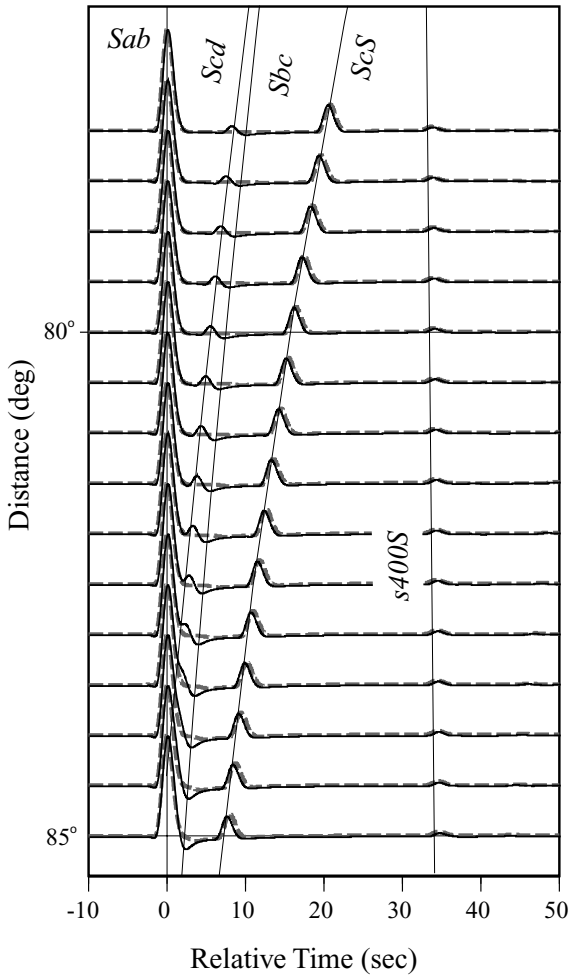

Figure 1. Transverse component displacement synthetics are shown for a 500 km deep event at teleseismic ranges. The calculation is done for a D″ discontinuity model with a 1.3 per cent V_S increase located 264 km above the CMB (solid lines), and for PREM (dashed lines). Synthetics are aligned and normalized to unity on the phase *S*, and calculated for a dominant period of 4 s. Phase labels are given for the D″ model, noting that the PREM model does not display the triplication phase *SdS*. Note, the phase SdS is composed of the two arrivals *Scd* (positive peak) and *Sbc* (positive and negative peak immediately following *Scd*).

spherical wave fronts and geometrical rays, which are perpendicular to the wave fronts, can be seen. Infinite frequency ray paths are useful for visualizing the path that seismic energy takes through the mantle, however, the seismic energy interaction with Earth structure surrounding the geometric ray must be considered because it also contributes energy to the seismic phases recorded at the surface (e.g. Dahlen *et al.* 2000).

1.3 Study objectives

Observations demonstrate that D″ structure varies laterally on many scales and this is also true for the D″ discontinuity. Because D″ discontinuity topography and V_S heterogeneity are both likely to be 3-D in nature (e.g. Tackley 2000; Farnetani & Samuel 2005), there are major challenges in resolving discontinuity topography from surrounding volumetric velocity heterogeneity. Moreover, many D″ discontinuity structures have been inferred based on using localized 1-D processing techniques, without it being clear how to generalize

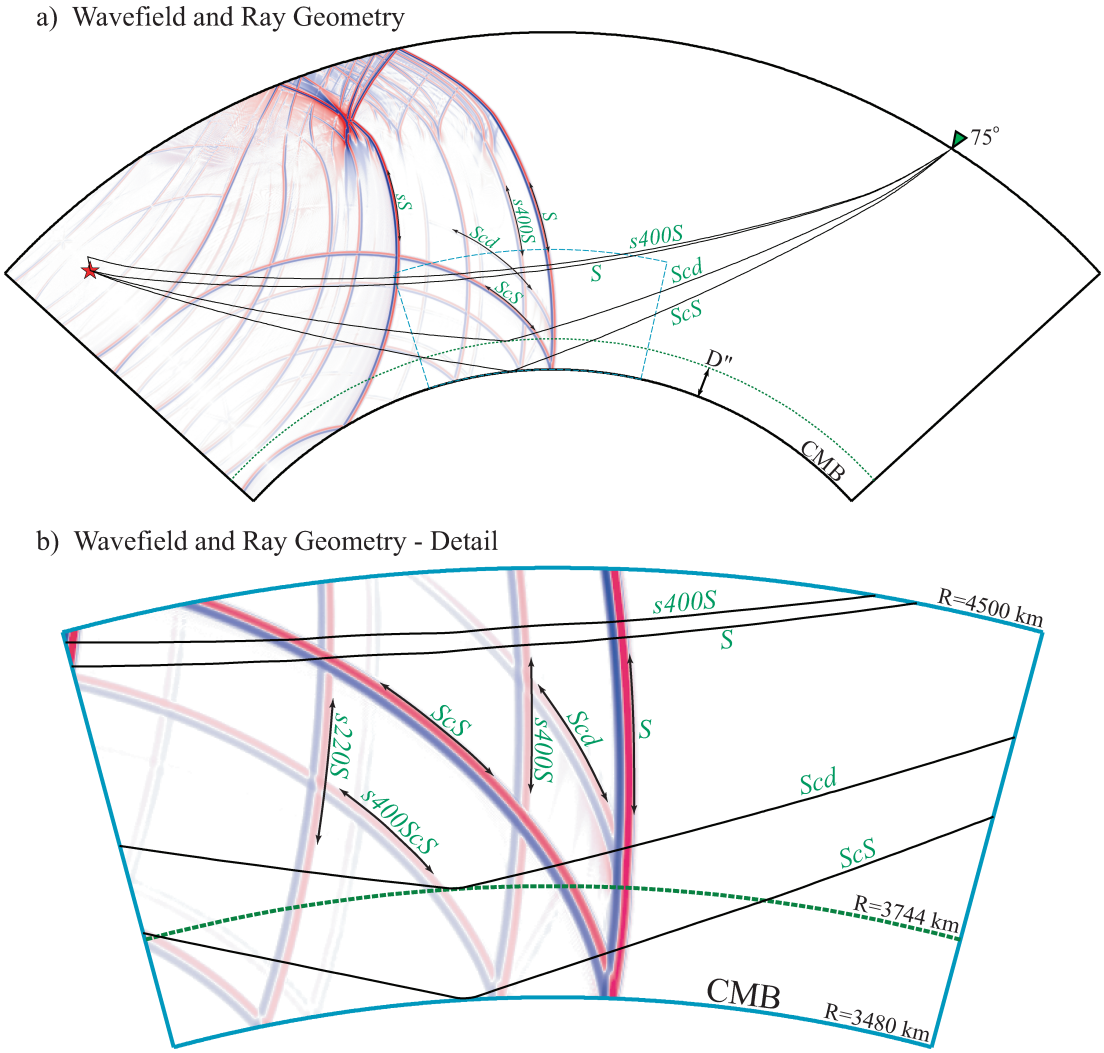

Figure 2. (a) The *SH*- velocity wavefield is shown at propagation time of 600 s for a 500 km deep event with dominant source period of 6 s. Selected wave fronts are labelled with black double-sided arrows. Ray paths are drawn in black for an epicentral distance of 75°. The calculation is done for the D″ discontinuity (indicated with a dashed green line) model of Fig. 1. Non-linear scaling was applied to the wavefield amplitudes to magnify lower amplitude phases. (b) Detail of wavefield shown in panel a. The region displayed is indicated by a dashed blue box in panel a.

those models to 3-D structures. This is particularly problematic for triplication arrivals that graze the deep mantle, with extensive horizontal averaging of the structure. 3-D models have been obtained directly using migration approaches that assume homogeneous reference structures and point-scattering assumptions, which intrinsically bias the model images. Tomography methods usually do not account for abrupt velocity discontinuities, and incur errors by incorrect back-projection of traveltimes on incorrect ray paths.

In order to progress from 1-D processing and modelling techniques that use simplifying assumptions for 3-D modelling, seismologists must use advanced synthetic seismogram techniques. Numerical techniques for computing synthetic seismograms in 2- or 3-D are now becoming practical because of the recent availability and processing power of cluster computing. We compute synthetic seismograms for cross-sections of laterally varying D″ discontinuity models beneath the Cocos Plate. This region has been extensively investigated because of excellent data coverage provided by South American events recorded at broad-band networks in California. We also create synthetic seismograms through cross-sections of a recent *S*-wave tomography model (Grand 2002). The models for which we construct and compute synthetics are summarized in Table 1. We compare waveforms and traveltime differentials from the computed synthetic seismograms with each other and double-array stack these synthetics for comparison with broad-band data used in the studies of Lay *et al.* (2004b) and Thomas *et al.* (2004a). Furthermore, we assess the challenges of using localized 1-D processing techniques and lateral extrapolations to infer laterally varying D″ discontinuity structure.

2 AXISYMMETRIC FINITE DIFFERENCE METHOD AND VERIFICATION

Constraining laterally varying D″ structure would ideally involve computation of synthetic seismograms for fully 3-D structures. However, techniques for computing synthetic seismograms for global 3-D geometries (e.g. SPECFEM3D; Komatitsch & Tromp 2002) are computationally intensive and cannot yet be readily

Table 1. Models.

Model	Description	Model based on
LAYB[a]	Block style bins	Lay *et al.* (2004b)
LAYL[a]	Linear interpolation between bins	Lay *et al.* (2004b)
THOM1.0[b]	1 per cent V_s increase beneath discontinuity	Thomas *et al.* (2004a)
THOM1.5[b]	1.5 per cent V_s and 1 per cent ρ increase beneath discontinuity	Thomas *et al.* (2004a)
THOM2.0[b]	2 per cent V_s increase beneath discontinuity	Thomas *et al.* (2004a)
TXBW	Tomographically derived δV_S heterogeneity	Grand (2002)

[a]Fixed D″ thickness, variable D″ δV_S.
[b]Variable D″ thickness, fixed D″ δV_S.

applied at the frequencies necessary (4–5 s) to model broad-band data. Hybrid approaches, where full 3-D geometries can be implemented in a subset of the globe (e.g. the coupled mode and spectral element approach, Capdeville *et al.* 2003), are promising for computing synthetics with shorter dominant periods using fully 3-D model geometries in the region of interest. A recent application by Toh *et al.* (2005) modelled the lowermost 370 km of the mantle in 3-D, pushing the calculations to dominant periods of 8 s. In order to attain shorter dominant periods we use the axisymmetric spherical Earth finite difference method (SHaxi) (based on Igel & Weber 1995, 1996; and extended in Jahnke *et al.* 2006) and explore laterally varying D″ structure beneath the Cocos Plate guided by recent data analyses. The SHaxi method is a powerful tool for investigating numerous models under the rotationally symmetric (RS) model assumption. This is the first application of the SHaxi method to data.

The SHaxi method uses a model defined on a 2-D cross-section grid in the vertical plane containing the great circle arc and is expanded to 3-D spherical geometry by (virtually) rotating the grid around the radial axis through the source. As a consequence, the computation on a 2-D grid provides seismograms with correct 3-D geometrical spreading, but only for RS geometries. This axisymmetric method has several advantages for computing synthetic seismograms. Because it computes the wavefield on a 2-D grid, synthetic seismograms can be generated for much shorter dominant periods (e.g. down to 1 s) than with full 3-D techniques. SHaxi also maintains the correct 3-D geometrical spreading for a spherical Earth, which is an advantage over purely 2-D techniques that do not. Because this scheme is a mixture between a 2-D method (in terms of storage needed for the seismic model and wavefield calculations) and a 3-D method (since point sources with correct 3-D spreading are modelled) this can be called a 2.5-D method.

The main restriction in using the SHaxi method is that structures incorporated on the 2-D axisymmetric grid are effectively mapped into 3-D ring-like structures (see Jahnke *et al.* 2006). This precludes modelling focusing and defocusing effects due to variations out of the great circle plane, but full wavefield behaviour within the great circle plane is accounted for including any multipathing, diffraction, or focusing. Given the very limited observational constraints on laterally varying D″ structure, it is usually not viable to define 3-D structures anyway. Additionally, the source acts as a strike-slip double couple with a fixed *SH* source radiation pattern proportional to the sine of the takeoff angle. This fixed radiation pattern makes direct comparison of amplitudes between synthetics and data from arbitrarily oriented sources slightly complicated. In this study, we are primarily concerned with differential travel time effects and overall waveform characteristics, but we do account for the radiation pattern effect when the synthetics are double array stacked.

In order to produce synthetic seismograms at relatively high frequencies we used 16 nodes (128 processors) of the Hitachi SR8000 super computer at the Leibniz-Rechenzentrum, Munich, Germany. These computations require 42 000 (lateral) × 6000 (radial) finite difference gridpoints. This grid spacing corresponds to roughly 0.5 km between gridpoints radially, and varies between 0.5 km (Earth's surface) and 0.25 km (CMB) laterally. Calculations are run to 1700 s of simulation time, which takes approximately 24 hr to compute. For these input parameters, synthetic seismograms with a dominant period of 4 s are produced. This is suitable for comparison with our *SH* observations which have been low-pass filtered with a cut-off of 3.3 s.

In order to ensure that our computations are accurate for the time and epicentral distance windows used in this study, we used the Gemini (Green's function of the Earth by Minor Integration) method of Friederich & Dalkolmo (1995) to compute PREM synthetics for comparison to our finite-difference results. The Gemini method was chosen because it has previously been used for verification of other synthetic seismogram techniques (Igel *et al.* 2000). Overlaying individual traces displays excellent agreement between the SHaxi and Gemini methods [a comparison of synthetics from both methods is shown in Supplemental Fig. A, available in the online version of the journal].

In synthetics created for PREM (Supplemental Fig. B), crustal and mid-crustal reverberations interfere with the *SdS* arrival. The average crustal structure represented in PREM is not a realistic estimate of the complex crustal structure beneath southern California recording stations (e.g. Zhu & Kanamori 2000). In order to compare our synthetics to data from southern California stations, we remove the crustal layers from PREM before computing synthetic seismograms.

3 STUDY REGION AND MODEL CONSTRUCTION

3.1 D″ structure beneath the Cocos Plate

The D″ discontinuity structure beneath the Cocos Plate region has been the focus of numerous seismological studies. Thomas *et al.* (2004a) provide a review of these studies, noting that a D″ *S*-wave velocity discontinuity has been consistently inferred at a height ranging between 150 and 300 km above the CMB with a velocity increase ranging from 0.9 to 3.0 per cent.

Recent studies have attempted to assess possible small-scale 2- or 3-D variability of the D″ shear velocity discontinuity beneath the Cocos Plate. Lay *et al.* (2004b), Thomas *et al.* (2004a) and Hutko *et al.* (2006) produced D″ discontinuity models for the Cocos Plate region using various stacking and migration methods. We compute synthetic seismograms through cross-sections of our laterally varying constructions of the models produced by Lay *et al.* (2004b) and

Thomas *et al.* (2004a). The 2.5-D approximation proves valid because the constraints on the structure tend to vary primarily with distance along narrow corridors; any attempt to extrapolate to a truly 3-D model is not justified by observations. We also compute synthetic seismograms for the tomography model of Grand (2002) for comparison. The variations in the tomography model are gradual enough that 2-D sections are good approximations to the structure locally sampled in a given corridor. We summarize below how we produced model cross-sections for use in the SHaxi method, and the results of comparing data to the resulting synthetics.

3.2 Double-array stacking model

Lay *et al.* (2004b) analysed broad-band transverse component seismograms including *SdS* and *ScS* arrivals from 14 deep South American events recorded by Californian regional networks. Fig. 3(a) shows the source–receiver geometries used. The study employed the double-array stacking technique of Revenaugh & Meyer (1997) to obtain apparent reflector depths of *SdS* energy for localized bins of data with nearby *ScS* CMB reflection points. Fig. 3(b) shows detailed outlines of the four geographic bins in which Lay *et al.* (2004b) grouped their data. They modelled the data using localized 1-D models, allowing the average velocity in the D″ layer to vary as needed to match the amplitude of *SdS,* finding that the variations required to match the amplitude kept the depth of the discontinuity almost constant. Their final model involved a 264 km thick D″ layer with varying V_S increase across the D″ layer ranging from 0.9 to 2.6 per cent. There is no direct basis for extrapolating this model into more than slightly different 2-D models sampled by a few offset ray paths.

To create models for use with the SHaxi method based on the localized 1-D results of Lay *et al.* (2004b), we construct cross-sections through four average great circle paths from source clusters to station clusters (Paths 1–4, Fig. 3b). These great circle paths are based on the average event–receiver location for events that have *ScS* bounce points in each of the four geographic bins. For each cross-section, we use PREM velocities above the D″ discontinuity. A brief description of models and their naming convention are outlined in Table 1. We constructed models with two end-member scenarios: (1) the velocity structure in each bin is block-like (model LAYB) (Supplemental Fig. C) and (2) the velocity structure is linearly interpolated between the centre of each bin (model LAYL). We use the same great circle paths (Paths 1–4) to construct cross-sections for the models listed in Table 1. We note that this process assumes very localized sensitivity of the 1-D modelling as implied by the fine binning used; as found below this results in very small-scale variations that are at odds with the intrinsic resolution of the nearly horizontally grazing ray geometry.

3.3 Point-scattering migration model

Thomas *et al.* (2004a) employed a pre-critical point-scattering migration technique (Thomas *et al.* 1999) to image the deep mantle beneath the Cocos Plate using the same data set as Lay *et al.* (2004b). The imaged model space was along a corridor roughly 700 km in length and 150 km wide (study region T shown in Fig. 3b), slightly oblique to the ray path coverage. The migration study used the 1-D background model ak135 (Kennett *et al.* 1995) to provide traveltimes for stacking windows of seismogram subsets compatible with scattering from a specified 3-D grid of scattering positions.

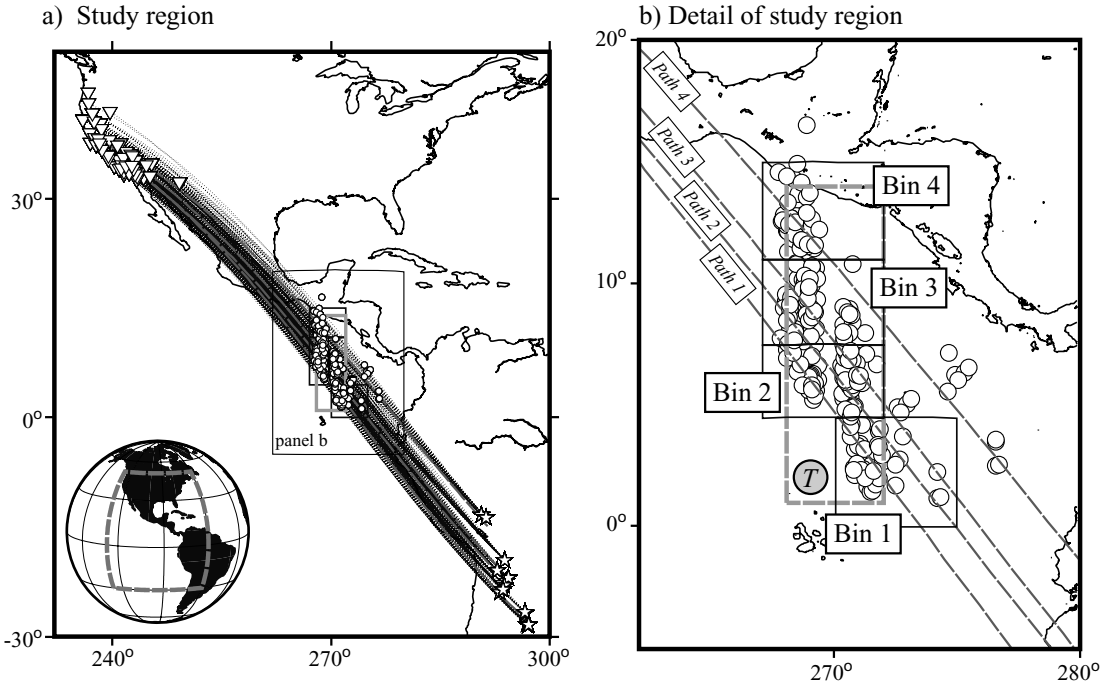

Figure 3. Location of study region. Panel (a) shows the general location of the study region. Shown are events (stars), receivers (triangles) event–receiver great circle paths (dashed lines) and *ScS* bounce points (circles) used in the studies of Lay *et al.* (2004b) and Thomas *et al.* (2004a). *ScS* bounce points are calculated from the PREM model. Both studies utilize the same data set. Panel (b) displays a detailed section of the study region. This panel shows the *ScS* bounce points as white circles. 1-D models were produced in the study of Lay *et al.* (2004b) for 4 distinct bins outlined in this plot by black rectangles (labelled Bins 1–4). The dashed grey lines (labelled Paths 1–4) represent the average great circle paths of source–receiver pairs for these four Bins, and are also the Paths for which we calculate synthetics in this study. The dashed grey rectangle (labelled with a grey-shaded T) represents the area modelled in the study of Thomas *et al.* (2004a).

V_S was not allowed to vary laterally, which projects all travel time variations into apparent scattering locations within the background model. A smoothed version of the resultant scattering image gives a topographically varying D″ discontinuity surface with a south-to-north increase in discontinuity height above the CMB from 150 to 300 km. The 150 km increase in discontinuity height occurs in the centre of the image region (near Bin2 of Lay *et al.* 2004b), over a lateral distance of roughly 200 km. The central region, containing the transition in discontinuity depth, does not reflect strong coherent energy and there is uncertainty in the continuity of the structure. The specific topography in this model is dependent on the assumed 1-D background structure. The migration geometry is again such that there is little basis for lateral extrapolation of the structure into more than slightly different 2-D models sampled by a few offset ray paths.

The migration approach used by Thomas *et al.* (2004a) does not model the amplitudes, and like all Kirchhoff migrations, images a reflector embedded in the background model without accounting for wave interactions with the structure. In order to compute synthetic seismograms for this structure, it is necessary to prescribe the V_S increase across the imaged reflector. Previous 1-D modelling efforts for the region suggested a 2.75 per cent (Lay & Helmberger 1983; Kendall & Nangini 1996) or 2.0 per cent (Ding & Helmberger 1997) V_S increase, but Lay *et al.* (2004b) suggest the region has strong lateral variability ranging from 0.9 to 2.6 per cent. As initial estimates, we chose V_S increases of 2.0 per cent (model THOM2.0) and 1.0 per cent (model THOM1.0).

Recent studies of a lower-mantle phase transition from magnesium silicate perovskite to a post-perovskite (ppv) structure indicate that the phase transition should involve 1.5 per cent V_S and 1 per cent density increases (Tsuchiya *et al.* 2004a), providing a possible explanation for the D″ discontinuity. This phase transition also is predicted to have a steep Clapeyron slope of ∼7–10 MPa K^{-1} (Oganov & Ono 2004; Tsuchiya *et al.* 2004b), which could account for significant topography on the D″ discontinuity. Because the study of Thomas *et al.* (2004a) suggests rapidly varying topography, as may accompany a ppv phase transition in the presence of lateral thermal and compositional gradients (e.g. Hernlund *et al.* 2005), we also create synthetic seismograms with 1.5 per cent V_S and 1 per cent density increases (model THOM1.5). Model cross-sections are shown in Supplemental Fig. C for model THOM2.0.

3.4 Tomography model

A consistent feature of recent *S*-wave tomography models (e.g. Masters *et al.* 1996; Kuo *et al.* 2000; Megnin & Romanowicz 2000; Ritsema & van Heijst 2000; Gu *et al.* 2001; Grand 2002) is the presence of relatively high shear velocities beneath the Central America and Cocos Plate region. Model TXBW (parametrized with 2.5° × 2.5° bins—roughly 150 km on a side) from Grand (2002) was not developed using triplication arrivals and resolves longer wavelength structure than models produced by Lay *et al.* (2004b) and Thomas *et al.* (2004a). The reference model for TXBW has relatively high D″ velocities, and the lowest layer (bottom 220 km of the mantle) in model TXBW contains high V_S perturbations (up to ∼2.3 per cent increases) relative to PREM beneath the Cocos Plate, with a general south-to-north velocity increase. This is consistent with the results of Lay *et al.* (2004b).

Ni *et al.* (2000) utilized the WKM method (a modification of the WKBJ method of Chapman 1978) to produce synthetic seismograms through 2-D cross-sections of block-style tomography models. As an application of their method, Ni *et al.* (2000) produced synthetics through two cross-sections of Grand's (1994) tomography model, with great-circle paths passing through the Central American region. Ni *et al.* (2000) were not able to observe the *SdS* phase for Grand's model for the chosen great-circle paths without arbitrarily increasing the velocity perturbations in the lowermost layer of the model by a factor of 3. Their synthetics then compare favourably to broad-band *Scd* waveforms of Ding & Helmberger (1997) for the Cocos Plate region.

We created four cross-sections through Grand's more recent tomography model TXBW (Grand 2002) for synthetic seismogram construction with the SHaxi method. To create cross-sections, we mapped the heterogeneity in TXBW onto our 2-D finite difference grid using four-point inverse distance weighted interpolation between the V_S values given in the model. Our cross-section through great circle Path 1 (Fig. 3) is identical to one of the cross-sections used in the study of Ni *et al.* (2000).

Model TXBW is parametrized in layers of blocks with constant *S*-wave velocity perturbations (δV_S). As shown in Fig. 4, we observe a noticeable increase in average V_S between the two lowermost layers along each of our reference great-circle paths (Path1: +1.5 per cent; Path 2: +1.75 per cent; Path 3: +1.75 per cent and Path 4: +2.0 per cent; Fig. 4). Ni *et al.* (2000) referenced the heterogeneity in Grand's tomography model directly to PREM (S. Ni, private communication, 2005) rather than to the 1-D reference model actually used in Grand's inversion. When we use the 1-D reference model of Grand, with its velocity increase in the lowermost mantle, the tomographic models produces significant *SdS* energy from the boundary between the two lowermost layers and we find no need to arbitrarily enhance the structure (Cross-sections are shown in Supplemental Figs D and E). Cross-sections through model TXBW show moderate variation in V_S progressing between Paths 1–2–3–4. The strongest variation in velocity structure is observed between Path 1 and 4. For model TXBW we did not remove the crust as was done in the other models that contained a simple PREM crust. The gradients in the tomography model structure are stronger along the ray path directions than perpendicular to the ray paths, so out-of-plane effects are expected to be relatively unimportant for this particular path geometry.

4 SYNTHETIC SEISMOGRAM RESULTS

We computed synthetic seismograms for each great-circle path through the three models described in the preceding section. Significant variability in waveform shape and differential traveltimes between seismic phases is found in the synthetic seismograms for the various models, as we discuss below. We consider $T_{ScS-Scd}$ and $T_{ScS-Sab}$, Scd/ScS amplitude ratios, and waveform characteristics for the different predictions.

4.1 Models LAYB and LAYL

Synthetic seismograms were computed for models LAYB and LAYL which have block-like or linearly interpolated V_S structures, respectively. Differences in waveform shape or traveltime of arrivals between LAYB and LAYL are not observable for the 4-s dominant period of our synthetic seismograms. This is because the geographic bin size used by Lay *et al.* (2004b) is small compared with the wavelength of *S*-wave energy in the D″ region (bins are ∼2.5° wide in the great circle arc direction, or ∼5 wavelengths of a 4 s dominant

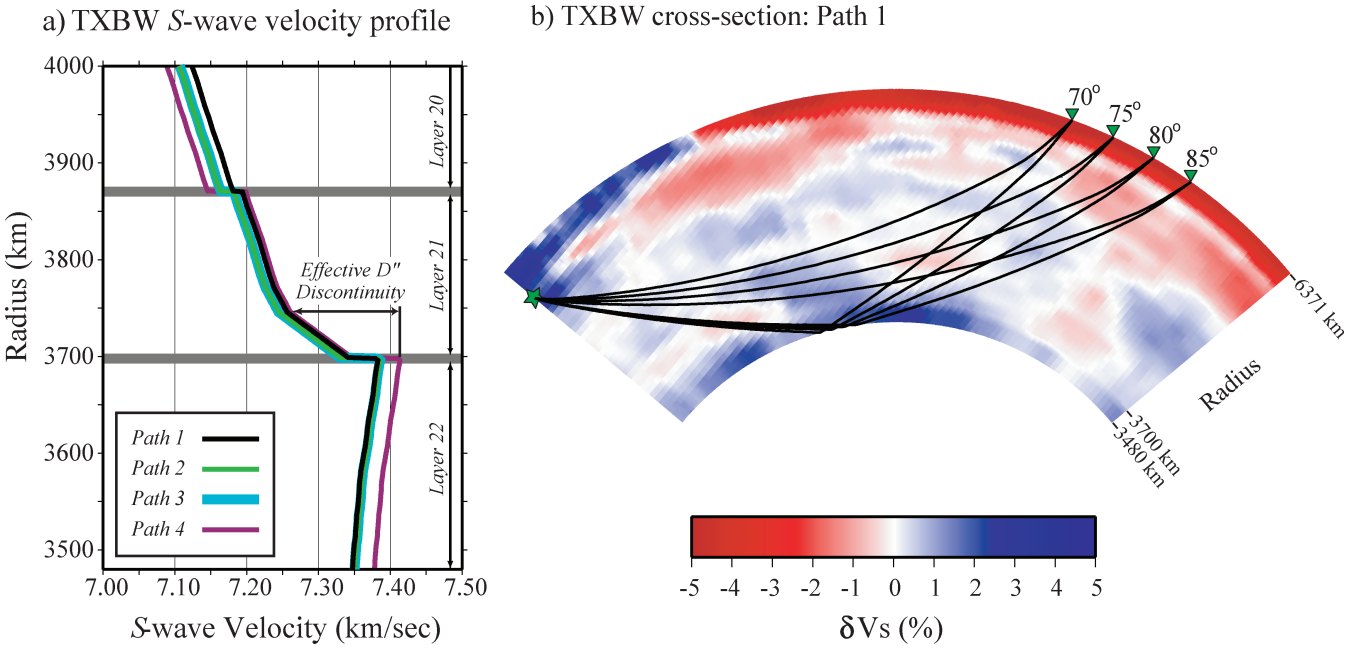

Figure 4. (a) V_S profile in the lower mantle through model TXBW. Shown is the 1-D V_S profile at an epicentral distance of 40°. This distance is chosen as approximating the central bounce point of *ScS* recorded at an epicentral distance of 80°. The profile is shown for Paths 1–4. Layer 20–22 refers to the layer number in the tomographic inversion of Grand (2002). The phase *SdS* is generated by an effective D″ discontinuity as indicated. (b) Whole mantle cross-section for Path 1 of model TXBW. Colour scaling is based on δV_S. Ray path geometry is shown for the phases *S* and *ScS* for a 500 km deep event (green star) recorded at receivers (green triangles) with epicentral distances 70°, 75°, 80° and 85°. Cross-sections for all paths through model TXBW are provided in Supplemental Fig. E.

period wave at the CMB). The effect of bin size on $T_{ScS-Scd}$ and $T_{ScS-Sab}$ will be discussed in Section 7.

We also compute synthetic seismograms for the 1-D models from Lay *et al.* (2004b) to compare with our synthetics for the cross-sectional interpolation of those models. Overlaying synthetics for model LAYB with synthetics for the 1-D models illuminates the laterally varying structural effects on waveform shape and timing (Supplemental Fig. F). Synthetics for model LAYB show simple *SdS* waveforms, similar to the 1-D predictions, with $T_{Scd-Sab}$ between the 1-D and RS models unchanged. However, there exists large variability in $T_{ScS-Scd}$ between the synthetics. This is not unexpected since *ScS* samples several bins in the RS computation, and thereby averages the laterally varying D″ structure. For example, RS predictions for Path 2 of LAYB show reduced $T_{ScS-Scd}$ (∼1.5 s decrease for 70°–80°) from those for the optimal 1-D model for Bin 2. This difference is due to *ScS* having its central bounce point in Bin 2 (with a 0.4 per cent V_S increase in the 1-D model), but the *ScS* wave also travels through Bins 1 and 3 (which have 0.9 and 0.7 per cent V_S increases throughout D″, respectively). Thus the RS $T_{ScS-Scd}$ is relatively reduced, since *ScS* is advanced by the neighboring bins. Path 3 similarly has a smaller $T_{ScS-Scd}$ (∼1.5 s decrease). This illustrates the challenge of how to interpret a suite of localized 1-D model results; the models need to be projected and averaged along the ray paths in a manner akin to tomography when constructing a model rather than being treated as local blocks as we have done.

In addition to the large variations between 1-D and RS predicted $T_{ScS-Scd}$ significant variations in *Scd*/*ScS* amplitude ratios are present. Only minor differences exist in predicted *ScS*/*Sab* amplitude ratios implying that differences in 1-D and RS *Scd*/*ScS* predictions are due to laterally varying effects on *Scd*. In general, increasing V_S below the D″ discontinuity increases *Scd* amplitudes. *Scd* amplitudes in the RS synthetics are sensitive to D″ velocities in the neighbouring bins because of the grazing ray geometry. For example, synthetics for Path 2 of LAYB show an increase in the *Scd*/*ScS* amplitude ratio over synthetics for the 1-D Bin 2 model (ratio increase from 0.07 to 0.15), owing to Bin 2 being adjacent to two higher velocity bins. This again suggests that mapping of localized 1-D structure into a RS model requires the models to be projected and averaged along the ray paths.

4.2 Models THOM1.0, THOM1.5 and THOM2.0

We constructed three models based on Thomas *et al.* (2004a), one for each of three distinct D″ velocities (see Table 1). Larger D″ velocity increases produce smaller $T_{ScS-Scd}$ and larger *Scd*/*ScS* amplitude ratios, which accounts for the main differences in synthetics for models THOM1.0, THOM1.5 and THOM2.0. Model THOM1.5 also included a 1 per cent density increase, which produced indistinguishable synthetics from those for models with density increases varying from 0 to 5 per cent.

Although differences between models THOM1.0 and THOM2.0 are straightforward, *ScS*–*Scd* differential timing and *Scd*/*ScS* amplitude ratio effects between Paths 1 and 4 are complex (Supplemental Fig. G). Here, we restrict the discussion of variable path effects to model THOM2.0.

Along Path 1, the wavefield encounters the deepest D″ discontinuity (∼130 km above the CMB) (see Supplemental Fig. C). Consequently, $T_{ScS-Scd}$ are the smallest. Along Path 4, the wavefield encounters the shallowest D″ discontinuity (∼290 km above the CMB). Although $T_{ScS-Scd}$ for Path 4 are greater than for Path 1 (ranging between 1.5 s larger at 80° to 9 s larger at 71°), the largest $T_{ScS-Scd}$ are sometimes observed for Paths 2 and 3. Along Paths 2 and 3 the wavefield encounters the transition from a deep to

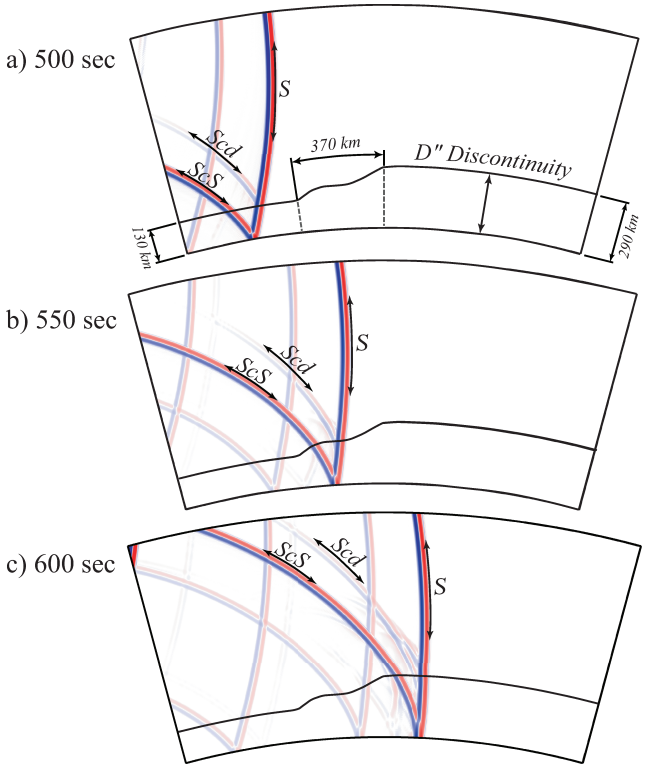

Figure 5. Snapshots at three time intervals are shown for model THOM2.0 for Path 3. The view displayed includes a section of the lower-most mantle between radii 3480 and 4500 km and between epicentral distances 25°–55°. The amplitude of the *SH*-velocity wavefield is shown in red and blue. The top of the D″ discontinuity in model THOM2.0 is drawn with a solid black line. Select seismic phases are labelled with double-sided arrows. These snapshots show the evolution of the wavefield as it encounters a D″ discontinuity with topographic variation. The topographic variation is observed to produce two distinct *Scd* arrivals.

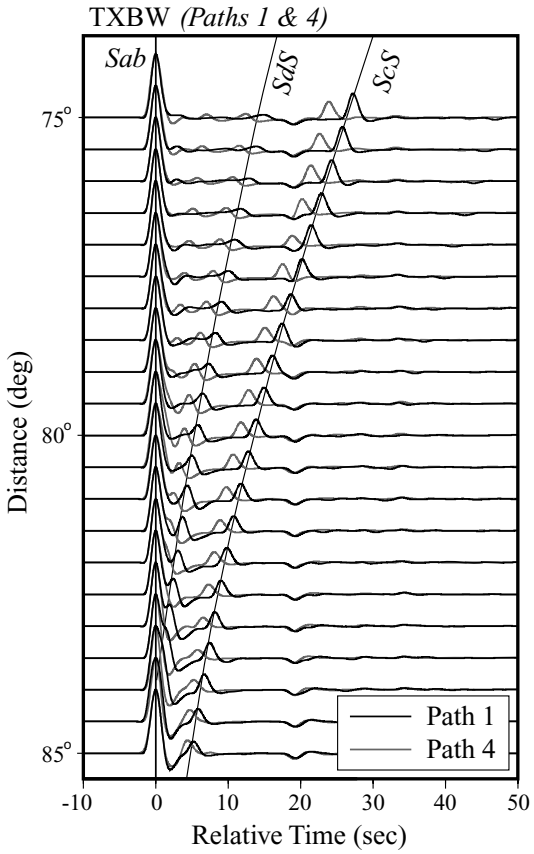

Figure 6. Comparison of synthetics for model TXBW for Paths 1 (black) and 4 (grey). Transverse component displacement synthetics are shown. Synthetics are aligned and normalized to unity on the phase *Sab*, and calculated for a dominant period of 4 s. For clarity, lines are drawn at the peak *SdS* and *ScS* arrival time for Path 1.

shallow D″ discontinuity. Three snapshots of the *SdS* and *ScS* portions of the wavefield are shown for Path 3 (Fig. 5), which displays the development of a double *Scd* arrival. In Fig. 5(a) as the wavefield interacts with the deepest D″ discontinuity structure the *Scd* phase is already apparent. 50 s later the wavefield interacts with the transition from a deep to shallow discontinuity (Fig. 5b), showing more *Scd* complexity due to multipathing. A double *Scd* arrival is fully developed 50 s later, apparent as two distinct *Scd* peaks in the synthetic seismograms.

At closer epicentral distances (from 70° to 72° for Path 3) the *Scd* arrival originating from the deeper discontinuity has higher amplitudes. At the further epicentral distances (>72° for Path 3) the *Scd* arrival originating from the shallower discontinuity has the higher amplitudes. Arrival times based on *Scd* peak amplitudes imply an abrupt jump in $T_{ScS-Scd}$ at the epicentral distance where *Scd* amplitudes from the shallower discontinuity overtake *Scd* amplitudes from the deeper discontinuity. For Path 3, a 3 s change in $T_{ScS-Scd}$ occurs at 72°.

4.3 Model TXBW

Fig. 6 shows overlain synthetic seismograms computed for model TXBW for Paths 1 and 4. A clear *SdS* arrival between *Sab* and *ScS*, as well as arrivals between *Sab* and *SdS* caused by crustal reverberations, are apparent for both models. Because of the layered block-style inversion used to create TXBW, other small arrivals are present from discontinuous jumps between layers.

Decreases in $T_{ScS-Sab}$ (generally <1 s on average, but up to 2 s between Paths 1 and 4) are observed moving from Path 1 to Path 4, due to progressively increasing V_S toward the north in the D″ region. This also decreases $T_{ScS-Scd}$ by <1 s on average between Path 1 and Path 4. 3-D structure elsewhere along the paths likely plays some role in timing and amplitude anomalies (e.g. Zhao & Lei 2004), but our focus here is on D″ structure. Nonetheless, we note variable *Scd*/*ScS* amplitude ratios that are not easily understandable in terms of D″ structure alone.

5 SYNTHETIC SEISMOGRAMS COMPARED WITH DATA

The most direct assessment of a model's performance is to compare the synthetic predictions with data. We compare synthetic predictions for Path 1 with the data set used in the studies of Lay *et al.* (2004b) and Thomas *et al.* (2004a). The four Bins used by Lay *et al.* (2004b) contained records spanning limited epicentral distance ranges. The ranges are: Bin 1: 79°–82°; Bin 2: 71°–79°; Bin 3: 75°–82° and Bin 4: 70°–77°. It is difficult to detect *SdS* in individual records for epicentral distances less than roughly 78°, because *Scd* amplitudes are relatively low at shorter distances and are often

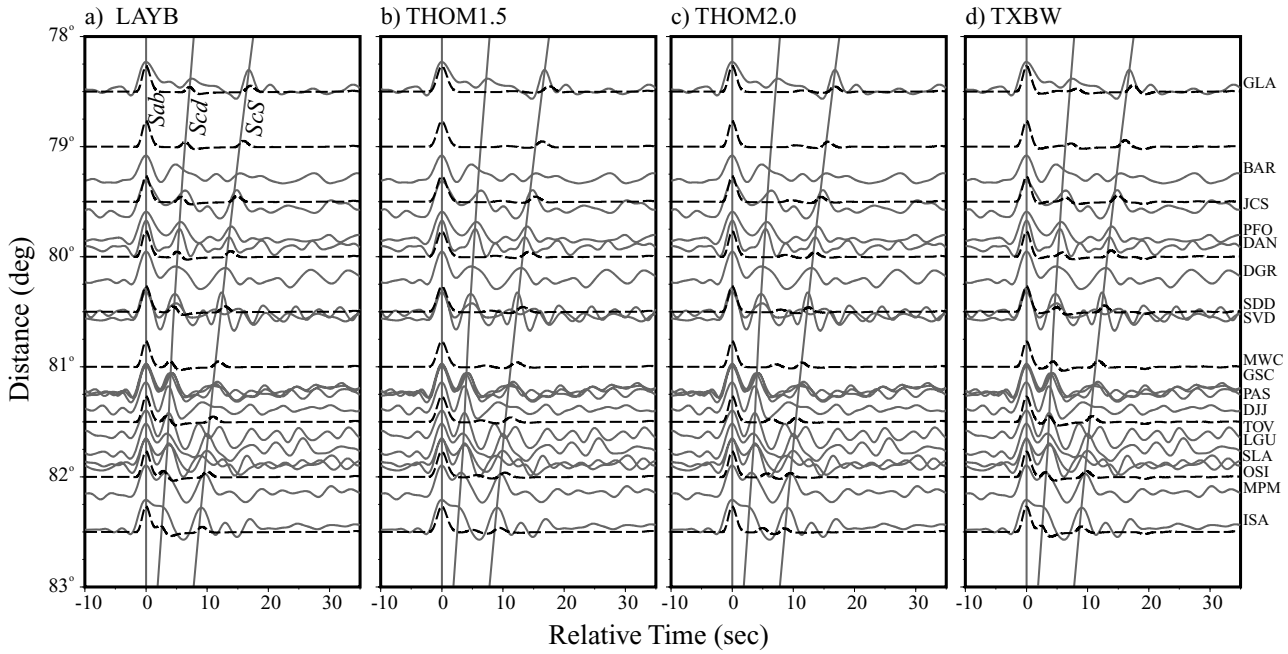

Figure 7. Comparison of synthetics created for Path 1 (dashed lines) with data (solid lines, 2000 April 23, Argentina 600 km deep event). Transverse component displacement synthetics and data are shown. Data are distance shifted to a source depth of 500 km. Approximate arrival times (peak amplitude) for the phases *Sab*, *Scd* and *ScS* for data are indicated by solid lines so that differences between data and synthetic differential traveltimes can be easily inspected visually. Receiver names are listed to the right of data traces.

obscured by noise in the traces (e.g. see Supplemental Fig. H). The inferred small D″ discontinuity V_S increase (e.g. 0.4 per cent for Bin 2, or 0.7 per cent for Bin 3) is a consequence of weak *SdS* energy in individual traces. These two factors make direct comparison of data with synthetics challenging for Paths 2, 3 and 4. Data grouped into Bin 1 show *SdS* energy in individual traces, allowing us to compare these recordings with synthetic seismograms for Path 1.

Fig. 7 shows synthetic seismograms for models LAYB, THOM1.5, THOM2.0 and TXBW along with data from the 2000 April 23, Argentina event. Although some scatter exists in traveltimes and amplitudes of *SdS* energy for signals grouped into Bin 1, the event shown in Fig. 7 is representative. As previously mentioned, the SHaxi method has a fixed source radiation pattern, so amplitude differences in the phases shown in Fig. 6 are not exactly comparable, with the synthetics expected to show relatively low *ScS*/*Sab* amplitude ratios due to the effective source radiation pattern.

Model LAYB (Fig. 7a) adequately explains $T_{ScS-Scd}$, although $T_{ScS-Sab}$ are slightly too large. Model THOM1.0 (not shown in Fig. 7) reproduces $T_{ScS-Scd}$ the best amongst the models based on Thomas *et al*. (2004a) but does not predict $T_{ScS-Scd}$ as well as model LAYB. Model THOM1.5 (Fig. 7b) performs better than model THOM2.0 in reproducing $T_{ScS-Scd}$; however, model THOM1.5 does worse than THOM2.0 in predicting the $T_{ScS-Sab}$ differential times. Model THOM2.0 (Fig. 7c) predicts $T_{ScS-Sab}$ differential times accurately, but underpredicts $T_{ScS-Scd}$ by as much as 2.5 s. The best agreement between synthetics and data for Path 1 is observed for model TXBW (Fig. 7d). $T_{ScS-Sab}$ and $T_{ScS-Scd}$ are in excellent agreement, particularly for distances greater than ∼80°. TXBW slightly overpredicts $T_{ScS-Sab}$ for distances less than 80°, however, $T_{ScS-Scd}$ is well matched. Differential travel times $T_{ScS-Sab}$ and $T_{ScS-Scd}$ for all data and synthetic models for Bin/Path 1 are plotted in Supplemental Fig. I.

6 DOUBLE-ARRAY STACKING COMPARISONS

Because it is generally difficult to observe the *Scd* phase in individual records for distances less than 78°, the studies of Lay *et al.* (2004b) and Thomas *et al.* (2004a) employed data stacking techniques to infer D″ discontinuity properties. Here we stack synthetic seismograms using the double-array stacking technique of Revenaugh & Meyer (1997) to obtain apparent reflector depths of the *SdS* energy (as in Lay *et al.* 2004b). The SHaxi method has a fixed source radiation pattern, and we can predict its effect on the amplitudes of resulting stacks. All that is needed is to slightly scale *ScS* relative to *SdS* in the stacking of synthetics by normalizing *ScS* in the synthetics on a value less than unity by an amount corresponding to the ratio of the radiation pattern coefficient for *ScS* divided by that for *SdS*. The actual data are not scaled for source radiation pattern because for each bin the average *SdS*/*ScS* corrections are very close to 1.0.

Fig. 8 shows double-array stacks of data compared to synthetic predictions, as functions of target depth relative to the CMB. PREM is used as the reference stacking velocity model for both data and synthetics, so apparent *SdS* reflector depths are biased to the same extent. We stack synthetics for the same ranges of epicentral distance as those of the corresponding data. *ScS* energy stacks coherently at the CMB because the *ScS* peaks are aligned on the reference *ScS* arrival times. *SdS* energy is clearly apparent in the data stacks at the apparent depths indicated by the arrows. Saw tooth irregularities at shallower depths occur as a result of individual waveform truncation before the *Sab* arrival. This is done because there tends to be a rise in amplitude of the traces in the *Sab* coda.

Double-beam stacking results are summarized in Table 2. Model THOM1.0 predicts the apparent D″ discontinuity depth best, however, it under predicts the *SdS*/*ScS* amplitude ratio most severely.

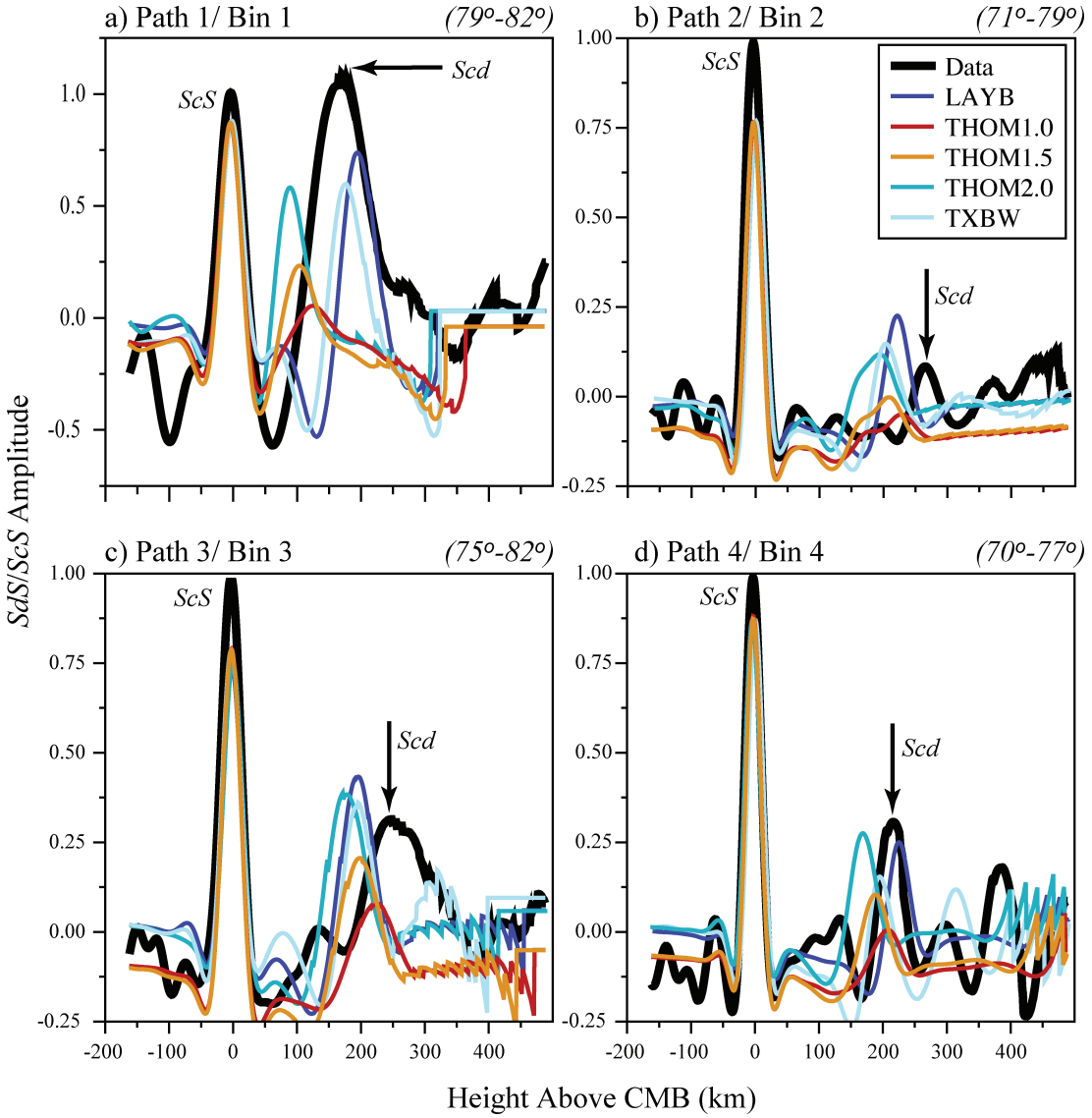

Figure 8. Stacking results for each Path (1–4) of synthetic prediction and Bin (1–4) of data are shown. Data stacks from Lay *et al.* (2004b) are drawn in black. The epicentral distance range of these data is displayed in the upper right corner of each panel. We stacked synthetic seismograms for the same epicentral distance range as these data.

Table 2. D″ thickness (km)[a] from double-beam stacking for data and models.

Path	Data	LAYB	THOM1.0	THOM1.5	THOM2.0	TXBW
Path 1	160	185	115	95	80	167
Path 2	270	227	234	215	200	210
Path 3	250	196	230	202	182	198
Path 4	220	229	213	193	172	199

[a]Thickness refers to *Scd* peak in Fig. 8.

Overall, models LAYB and TXBW predict combined apparent D″ discontinuity height and *SdS*/*ScS* amplitude ratios the best. Model THOM2.0 predicts the *SdS*/*ScS* amplitude ratio as well as models LAYB and TXBW, but it under predicts the discontinuity height the most, and the *SdS* waveform shapes are irregular. None of the matches are as good as for the 1-D models for each bin obtained by Lay *et al.* (2004b).

Although synthetics for model TXBW compare well with data, the fit is not perfect, especially for Path 2 (Fig. 8). D″ V_S likely varies on shorter scale lengths than TXBW is able to resolve, as suggested by the short-scale velocity variation of Lay *et al.* (2004b). It may be possible to obtain better synthetic-data agreement by slightly modifying model TXBW. The models of Lay *et al.* (2004b) can guide the direction such enhancements take, however, we found no simple procedure to map the structures suggested by Lay *et al.* (2004b) onto TXBW. Significant trial-and-error forward modelling, guided by the 1-D stacking results and the spatial distribution of the tomography model appears to be the best way to formulate the search for a best-fitting model.

The stacks shown in Fig. 8(a) are in agreement with the results of comparing individual synthetics to data records as in Fig. 7. That is, we can see that model TXBW indicates a reflector at the same height above the CMB as the data, while model LAYB suggests the height above the CMB to be slightly higher than the data suggest. The LAYB result can be understood in that the model produced a slight

overprediction of the *ScS–Scd* differential traveltimes. The underpredicted *ScS–Scd* differential traveltimes of models THOM1.0-THOM2.0 are manifested in the stacks of Fig. 8(a) as deeper D″ discontinuity reflectors than what these data suggest.

7 DISCUSSION

Our main focus has been to assess how well the laterally varying models inferred from various data analysis procedures actually account for the original observations. In this section, we discuss important sources of uncertainty and difficulties associated with the models for which we computed synthetic seismograms.

Lay *et al.* (2004b) produced 1-D models of the D″ discontinuity structure with excellent agreement to data stacks. However, our RS synthetics for model LAYB compared less favourably to data stacks. The main issue here is how best to develop a laterally varying structure from the 'local' characterization provided by small bin processing given the grazing nature of the seismic waves which must laterally average the structure. The *SdS* features in the data stacks are remarkably discrete; even small overlap of the bins leads to appearance of double peaks in the stacks, as noted by Lay *et al.* (2004b). However, the grazing ray geometry argues that this cannot be interpreted as resolving spatial heterogeneities on the same scale as the binning. What is needed is an understanding of the mapping of the locally characterized wavefield into laterally extensive heterogeneous structure. This is undoubtedly a non-linear mapping, given that volumetric heterogeneity and reflector topography can trade-off.

We explore the effects of V_S heterogeneity scale length on $T_{ScS-Scd}$ and $T_{ScS-Sab}$ in Fig. 9. We construct a suite of models with a base model containing a D″ discontinuity at a height of 264 km above the CMB and a V_S increase of 2.33 per cent. Synthetic seismograms are computed for a source 500 km deep at an epicentral distance of 78°. The *ScS* bounce point for this source–receiver geometry is located 38.12° from the source. Centred on this *ScS* bounce point we introduce a domain with higher V_S (+3 per cent increase). This higher velocity domain is given an extent along the great-circle path in varying multiples of the *ScS* wavelength for a dominant period of 7 s (1 wavelength ≈50 km). In Fig. 9, the *ScS–Sab* differential travel times are shown as a function of lateral extent for the high velocity region. For $T_{ScS-Sab}$, a domain extent of 2–3 wavelengths already affects the differential traveltimes by a few tenths of seconds. However it is not until a domain extent of roughly 30 wavelengths (∼1500 km for a 7 s dominant period wave) is reached that $T_{ScS-Sab}$ converges to the traveltime prediction for a 1-D model with a 3.0 per cent V_S increase beneath the discontinuity. This is consistent with the long path length of *ScS* within the D″ layer, as indicated in Fig. 2. The travel time differentials shown in Fig. 9 are also identical to those predicted by ray tracing through the structure. This suggests that ray tracing techniques may be a valuable aid in projecting localized 1-D models into 2- and 3-D models as these techniques will provide improved reference travel times.

The Bin sizes used in the Lay *et al.* (2004b) study are on average roughly 3 wavelengths in length along the great circle path. If the structural variations have the same scale as the bin dimensions, Fig. 9 demonstrates that differential traveltimes may be significantly dominated by the neighbouring bin structure. *ScS–Scd* times suffer a similar lack of path isolation. These experiments argue that 1-D travel time modelling results are biased if along path lateral variability is shorter scale than about 30-wavelengths. However, our *SdS* data clearly display strong variation over distances of much less than

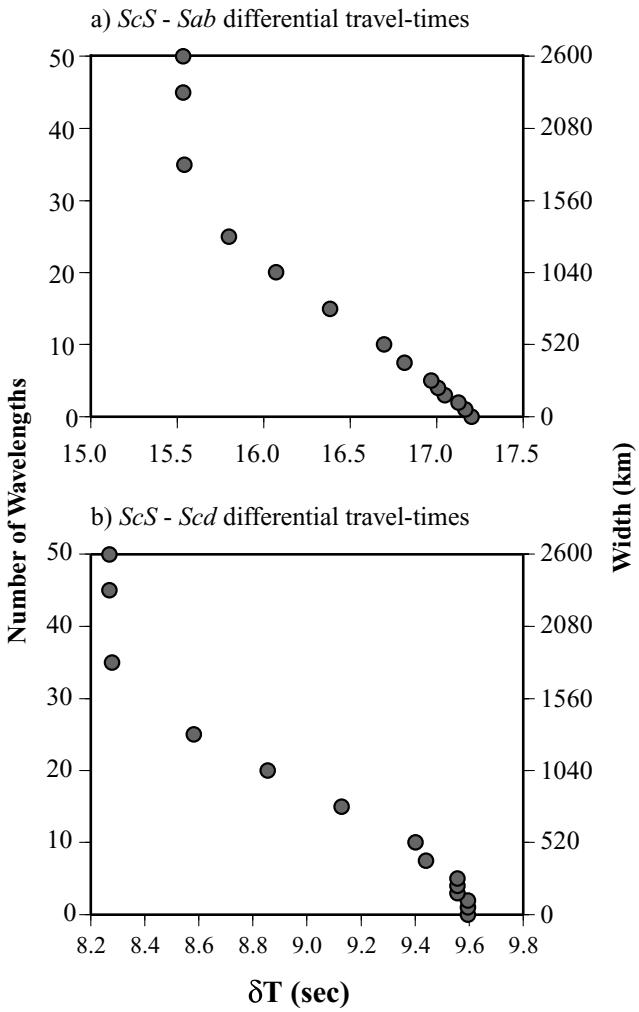

Figure 9. 3-D effects of D″ lateral V_S heterogeneity on $T_{ScS-Sab}$ (panel a) and $T_{ScS-Scd}$ (panel b) is shown. These differential traveltimes are computed for a D″ model with a constant $V_S = 7.375$ km s^{-1} (+2.33 per cent jump) except in a box centred on the *ScS* bounce point for source–receiver epicentral distance of 78° and source depth of 500 km (central bounce point = 38.12°). Inside this box the V_S is 7.431 km s^{-1} (+3 per cent jump). The D″ thickness is fixed at 264 km corresponding with the study of Lay *et al.* (2004b). The extent of the inner box along the profile is shown on the right axis in km and on the left axis in multiples of the wavelength of *ScS* in the box. The wavelength multiples are shown for a *ScS* dominant period of 7 s for which the synthetics were computed.

30-wavelengths, thus 2- or 3-D techniques must be employed to reliably map the required heterogeneous structure. It is unrealistically optimistic to believe that fine binning resolves fine scale structure when grazing rays are being used; the wave propagation effects may be spatially rapidly varying but the responsible structure is likely to be much larger scale. Since tomography intrinsically distributes path integral effects over large scale, it can provide a good starting basis for initial modelling, as demonstrated by Ni *et al.* (2000) and by the modelling in this paper.

Paths 2 and 3 of models THOM1.0-2.0 show a rapid transition in D″ discontinuity thickness (e.g. Fig. 5) producing a double *Scd* peak in the synthetic predictions. This double *Scd* peak has not been reported in observations for this region, but Gaherty & Lay (1992) have noted such features under Eurasia. Given the possibility of the post-perovskite phase transition being responsible for the D″

discontinuity, it is interesting to establish whether models with rapid variations in topography can account for the data. Future efforts seeking to resolve topographic variation on the D″ discontinuity should consider the prediction of a double *Scd* arrival.

For the SHaxi approach, out of great circle plane variations in D″ discontinuity topography is not modelled, so we do not model the exact scattering of energy that the full 3-D model of Thomas *et al.* (2004a) would produce. Because our models are axisymmetric, more *SdS* energy may be backscattered from the transition from thin to thick D″ layering in models THOM1.0-2.0 than would be scattered in fully 3-D models. Models THOM1.0-2.0 have relatively small *SdS*/*Scd* amplitudes, though we are not able to constrain the degree of *Scd* amplitude misfit due to our geometry. Perhaps the greatest challenge for interpreting migration images is that they do not resolve velocity contrasts (at least for Kirchhoff diffraction migrations), and the reflector images are highly dependent on the reference velocity structure. Volumetric heterogeneity as needed to match *ScS* arrival times suggests that the apparent topography is likely to be incorrect, and in this case, exaggerated. This uncertainty extends to any effort to infer dynamic features based on the migration images.

If V_S gradients perpendicular to our RS cross-sections for model TXBW are insignificant for a couple of wavelengths our synthetics should be adequate. Because there was only slight change in our synthetic predictions between individual paths, lateral variation does appears to be minor for our geometry and full 3-D synthetics may not be necessary to predict the waveforms in this case. Not having to compute full 3-D synthetics for the present class of whole Earth tomography models would drastically save computational resources and time, and is currently feasible using low-cost cluster computing. However, if strong lateral gradients in the tomography models velocity structure exist out of the great-circle plane fully 3-D techniques should be employed (e.g. Toh *et al.* 2005).

8 CONCLUSIONS

We have demonstrated that important wavefield effects are predicted for models of laterally varying D″ structure built upon underlying 1-D modelling assumptions. We have investigated recent models of D″ discontinuity structure beneath the Cocos Plate region using RS synthetic seismograms calculated with the finite-difference SHaxi method. We made synthetic predictions for models inferred from results of several recent 'high resolution' imaging studies, including D″ discontinuity mapping by stacking and migration, and tomographically derived volumetric heterogeneity. We focused our comparison on seismic phases predominantly used to image D″ discontinuity structure: *S*, *ScS* and the intermediate arrival *SdS,* which is present if a high velocity D″ layer exists. We found significant discrepancies between observations and synthetic predictions, which highlight the need for higher dimensional tools in the process of mapping localized imaging results into 3-D structure. 1-D tools are unable to accurately predict the RS structure if structural variations are on the order of wavelength of the energy used; the problem is particularly severe for grazing ray geometries. Ray tracing techniques may aid in constructing 3-D models by providing improved reference seismic arrival times. However, methods utilizing synthetic seismograms, such as the SHaxi approach, are better suited for this purpose as complete waveform effects can be synthesized robustly. In order to model fine-scale D″ structure, we believe future efforts should incorporate methods of synthesizing 2- or 3-D seismograms in an iterative approach. Reasonable starting models may be constructed by migration or double-array stacking techniques, which may be improved if tomographic models are used as the reference structure. Initial models can be improved in an iterative fashion by computing synthetic seismograms, comparing the synthetics with data, and adjusting the model. However, it will be challenging to determine the best way to adjust the model in the forward sense, requiring significant trial and error. The reality of data coverage limitations is that there is almost never good constraint on 3-D structural variations at the base of the mantle, so often 2-D attributes are all that can be inferred, and even this is tenuous. In the inverse sense, low cost methods such as SHaxi may allow reasonable full waveform inversions to be calculated along corridors densely sampled with data.

ACKNOWLEDGMENTS

Most figures were generated using the Generic Mapping Tools freeware package (Wessel & Smith 1998). We thank two anonymous reviewers and editor J. Trampert for their constructive comments which helped us to improve the paper. MT and EG were partially supported by NSF grant EAR-0135119. TL was supported by NSF Grant EAR-0125595. Thanks to the Leibniz Computing Center, Munich, for access to their computational facilities. Support is also acknowledged from the German Academic Exchange Service (IQN-Georisk), the German Research Foundation and the Human Resources and Mobility Programme of the European Union (SPICE-Project). The SHaxi source code is openly available at http://www.spice-rtn.org/.

REFERENCES

Avants, M.S., Lay, T., Russell, S.A. & Garnero, E.J., 2006. Shear-velocity variation within the D″ region beneath the central Pacific, *J. geophys. Res.,* **111,** B05305, doi:1029/2004JB003270.

Bullen, K.E., 1949. Compressibility-pressure hypothesis and the Earth's interior, *Mon. Not. R. astr. Soc.,* Geophysics Supplement, 355–368.

Capdeville, Y., To, A. & Romanowicz, B., 2003. Coupling spectral elements and modes in a spherical Earth: an extension to the 'sandwich' case, *Geophys. J. Int.,* **154,** 44–57.

Chapman, C.H., 1978. A new method for computing synthetic seismograms, *Geophys. J. R. astr. Soc.,* **54,** 481–518.

Creager, K.C. & Jordan, T.H., 1986. Aspherical structure of the core-mantle boundary from PKP Travel-Times, *Geophys. Res. Lett.,* **13,** 1497–1500.

Dahlen, F.A., Hung, S.H. & Nolet, G., 2000. Frechet kernels for finite-frequency traveltimes—I. Theory, *Geophys. J. Int.,* **141,** 157–174.

Ding, X.M. & Helmberger, D.V., 1997. Modelling D″ structure beneath Central America with broadband seismic data, *Phys. Earth planet. Int.,* **101,** 245–270.

Dziewonski, A.M. & Anderson, D.L., 1981. Preliminary Reference Earth Model, *Phys. Earth planet. Int.,* **25,** 297–356.

Farnetani, C.G. & Samuel, H., 2005. Beyond the thermal plume paradigm, *Geophys. Res. Lett.,* **32** (7), L07311, doi:10.1029/2005GL022360.

Flanagan, M.P. & Shearer, P.M., 1998. Topography on the 410-km seismic velocity discontinuity near subduction zones from stacking of sS, sP, and pP precursors, *J. Geophys. Res.-Solid Earth,* **103,** 21 165–21 182.

Friederich, W. & Dalkolmo, J., 1995. Complete synthetic seismograms for a spherically symmetrical Earth by a numerical computation of the Greens-function in the frequency-domain, *Geophys. J. Int.,* **122,** 537–550.

Gaherty, J.B. & Lay, T., 1992. Investigation of laterally heterogeneous shear velocity structure in D″ beneath Eurasia, *J. Geophys. Res.-Solid Earth,* **97,** 417–435.

Garnero, E.J., Helmberger, D.V. & Grand, S., 1993. Preliminary evidence for a lower mantle shear-wave velocity discontinuity beneaththe Central Pacific, *Phys. Earth planet. Inter.,* **79,** 335–347.

Garnero, E.J. & Lay, T., 1997. Lateral variations in lowermost mantle shear wave anisotropy beneath the north Pacific and Alaska, *J. Geophys. Res.-Solid Earth,* **102,** 8121–8135.

Garnero, E.J. & Lay, T., 2003. D″ shear velocity heterogeneity, anisotropy and discontinuity structure beneath the Caribbean and Central America, *Phys. Earth planet. Inter.,* **140,** 219–242.

Grand, S.P., 1994. Mantle shear structure beneath the America and surrounding oceans, *J. Geophys. Res.-Solid Earth,* **99,** 11 591–11 621.

Grand, S.P., 2002. Mantle shear-wave tomography and the fate of subducted slabs, *Philos. Trans. R. Soc. Lond. Ser. A-Math. Phys. Eng. Sci.,* **360,** 2475–2491.

Gu, Y.J., Dziewonski, A.M., Su, W.J. & Ekstrom, G., 2001. Models of the mantle shear velocity and discontinuities in the pattern of lateral heterogeneities, *J. Geophys. Res.-Solid Earth,* **106,** 11 169–11 199.

Hernlund, J.W., Thomas, C. & Tackley, P.J., 2005. A doubling of the post-perovskite phase boundary and structure of the Earth's lowermost mantle, *Nature,* **434,** 883–886.

Houard, S. & Nataf, H.C., 1993. Laterally varying reflector at the top of D″ beneath Northern Siberia, *Geophys. J. Int.,* **115,** 168–182.

Hung, S.-H., Garnero, E., Chiao, L.-Y., Lay, T. & Kuo, B.Y., 2005. Finite frequency tomography of D″ shear velocity heterogeneity beneath the Caribbean, *J. geophys. Res.,* **110,** doi:10.1029/2004JB003373.

Hutko, A., Lay, T., Garnero, E. & Revenaugh, J.R., 2006. Seismic detection of folded, subducted lithosphere at the core-mantle boundary, *Nature,* **441** (18), doi:10.1038, 333–336.

Igel, H. & Weber, M., 1995. SH–wave propagation in the whole mantle using high-order finite differences, *Geophys. Res. Lett.,* **22,** 731–734.

Igel, H. & Weber, M., 1996. P-SV wave propagation in the Earth's mantle using finite differences: Application to heterogeneous lowermost mantle structure, *Geophys. Res. Lett.,* **23,** 415–418.

Igel, H., Takeuchi, N., Geller, R.J., Megnin, C., Bunge, H.P., Clevede, E., Dalkolmo, J. & Romanowicz, B., 2000. The COSY Project: verification of global seismic modeling algorithms, *Phys. Earth planet. Inter.,* **119,** 3–23.

Jahnke, G., Thorne, M.S., Cochard, A. & Igel, H., 2006. Global SH wave propagation with an axi-symmetric finite-difference scheme, *Geophys. J. Int.,* submitted.

Kendall, J.M. & Shearer, P.M., 1994. Lateral Variations in D″ thickness from long-period shear-wave data, *J. Geophys. Res.-Solid Earth,* **99,** 11 575–11 590.

Kendall, J.M. & Nangini, C., 1996. Lateral variations in D″ below the Caribbean, *Geophys. Res. Lett.,* **23,** 399–402.

Kennett, B.L.N., Engdahl, E.R. & Buland, R., 1995. Constraints on seismic velocities in the Earth from travel-times, *Geophys. J. Int.,* **122,** 108–124.

Komatitsch, D. & Tromp, J., 2002. Spectral-element simulations of global seismic wave propagation—I. Validation, *Geophys. J. Int.,* **149,** 390–412.

Kuo, B.Y., Garnero, E.J. & Lay, T., 2000. Tomographic inversion of S-SKS times for shear velocity heterogeneity in D″: degree 12 and hybrid models, *J. Geophys. Res.-Solid Earth,* **105,** 28 139–28 157.

Lay, T. & Helmberger, D.V., 1983. A lower mantle S-wave triplication and the shear velocity structure of D″, *Geophys. J. R. astr. Soc.,* **75,** 799–837.

Lay, T. & Young, C.J., 1991. Analysis of seismic SV waves in the core's penumbra, *Geophys. Res. Lett.,* **18,** 1373–1376.

Lay, T., Garnero, E.J., Young, C.J. & Gaherty, J.B., 1997. Scale lengths of shear velocity heterogeneity at the base of the mantle from Swave differential travel times, *J. Geophys. Res.-Solid Earth,* **102,** 9887–9909.

Lay, T., Garnero, E.J. & William, Q., 2004a. Partial melting in a thermo-chemical boundary layer at the base of the mantle, *Phys. Earth planet. Inter.,* **146,** 441–467.

Lay, T., Garnero, E.J. & Russell, S.A., 2004b. Lateral variation of the D″ discontinuity beneath the Cocos Plate, *Geophys. Res. Lett.,* **31,** doi:10.1029/2004GL020300.

Lay, T., Hernlund, J., Garnero, E.J. & Thorne, M.S., 2006. A lens of post-perovskite and CMB heat flux in an iron-rich pile in D″ beneath the central Pacific, *Science,* **314,** 1272–1276.

Masters, G., Johnson, S., Laske, G. & Bolton, H., 1996. A shear-velocity model of the mantle, *Philos. Trans. R. Soc. Lond. Ser. A–Math. Phys. Eng. Sci.,* **354,** 1385–1410.

Matzel, E., Sen, M.K. & Grand, S.P., 1996. Evidence for anisotropy in the deep mantle beneath Alaska, *Geophys. Res. Lett.,* **23,** 2417–2420.

Megnin, C. & Romanowicz, B., 2000. The three-dimensional shear velocity structure of the mantle from the inversion of body, surface and higher-mode waveforms, *Geophys. J. Int.,* **143,** 709–728.

Ni, S.D., Ding, X.M. & Helmberger, D.V., 2000. Constructing synthetics from deep earth tomographic models, *Geophys. J. Int.,* **140,** 71–82.

Oganov, A.R. & Ono, S., 2004. Theoretical and experimental evidence for a post-perovskite phase of MgSiO3 in Earth's D″ layer, *Nature,* **430,** 445–448.

Revenaugh, J. & Meyer, R., 1997. Seismic evidence of partial melt within a possibly ubiquitous low-velocity layer at the base of the mantle, *Science,* **277,** 670–673.

Ritsema, J. & van Heijst, H.-J., 2000. Seismic imaging of structural heterogeneity in Earth's mantle: evidence for Large-Scale Mantle Flow, *Sci. Prog.,* **83,** 243–259.

Rokosky, J.M., Lay, T., Garnero, E.J. & Russell, S.A., 2004. High-resolution investigation of shear wave anisotropy in D″ beneath the Cocos Plate, *Geophys. Res. Lett.,* **31,** L07605.

Rost, S. & Revenaugh, J., 2003. Detection of a D″ discontinuity in the south Atlantic using PKKP, *Geophys. Res. Lett.,* **30,** 1840.

Sidorin, I., Gurnis, M., & Helmberger, D.V., 1999. Evidence for a ubiquitous seismic discontinuity at the base of the mantle, *Science,* **286,** 1326–1331.

Sun, D., Song, T.-A.R., & Helmberger, D.V., 2006. Complexity of D″ in the presence of slab-debris and phase changes, *Geophys. Res. Lett.,* **33,** L12807, doi:10.1029/2005GL025384.

Tackley, P.J., 2000. Mantle convection and plate tectonics: Towards an integrated physical and chemical theory, *Science,* **288,** 2002–2007.

Thomas, C., Weber, M., Wicks, C.W. & Scherbaum, F., 1999. Small scatterers in the lower mantle observed at German broadband arrays, *J. Geophys. Res.-Solid Earth,* **104,** 15 073–15 088.

Thomas, C., Garnero, E.J. & Lay, T., 2004a. High-resolution imaging of lowermost mantle structure under the Cocos plate, *J. Geophys. Res.-Solid Earth,* **109,** doi:10.1029/2004JB003013.

Thomas, C., Kendall, J. & Lowman, J., 2004b. Lower-mantle seismic discontinuities and the thermal morphology of subducted slabs, *Earth planet. Sci. Lett.,* **225,** 105–113.

Toh, A., Romanowicz, B., Capdeville, Y. & Takeuchi, N., 2005. 3D effects of sharp boundaries at the borders of the African and Pacific Superplumes: Observation and modeling, *Earth planet. Sci. Lett.,* **233,** 137–153.

Tsuchiya, T., Tsuchiya, J., Umemoto, K. & Wentzcovitch, R.A., 2004a. Phase transition in MgSiO3 perovskite in the earth's lower mantle, *Earth planet. Sci. Lett.,* **224,** 241–248.

Tsuchiya, T., Tsuchiya, J., Umemoto, K. & Wentzcovitch, R.M., 2004b. Elasticity of post-perovskite MgSiO3, *Geophys. Res. Lett.,* **31,** L14603, doi:10.1029/2004GL020278.

Valenzuela, R.W. & Wysession, M.E., 1998. Illuminating the Base of the Mantle with Diffracted Waves, in *The Core-Mantle Boundary Region,* pp. 57–71, eds Gurnis, M., Wysession, M.E., Knittle, E. & Buffet, B.A., American Geophysical Union, Washington, DC.

Weber, M. & Davis, J.P., 1990. Evidence of a laterally variable lower mantle structure from P-waves and S-waves, *Geophys. J. Int.,* **102,** 231–255.

Weber, M., 1993. P-wave and S-wave reflections from anomalies in the lowermost mantle, *Geophys. J. Int.,* **115,** 183–210.

Wessel, P. & Smith, W.H.F., 1998. New, improved version of the Generic Mapping Tools released, *EOS, Trans. Am. geophys. Un.,* **79,** 579.

Woodward, R.L. & Masters, G., 1991. Lower-mantle structure from ScS-S differential travel-times, *Nature,* **352,** 231–233.

Wysession, M.E., Lay, T., Revenaugh, J., Williams, Q., Garnero, E., Jeanloz, R. & Kellogg, L.H., 1998. The D″ discontinuity and its implications, in *The Core-Mantle Boundary Region,* pp. 273–297, eds Gurnis, M., Wysession, M.E., Knittle, E. & Buffet, B.A., American Geophysical Union, Washington, DC.

Young, C.J. & Lay, T., 1987. Evidence for a shear velocity discontinuity in the lower mantle beneath India and the Indian-Ocean, *Phys. Earth planet. Inter.,* **49,** 37–53.

Young, C.J. & Lay, T., 1990. Multiple phase analysis of the shear velocity structure in the D″ region beneath Alaska, *J. geophys. Res.,* **95,** 17 385–17 402.

Zhang, J.J. & Lay, T., 1984. Investigation of a lower mantle shear-wave triplication using a broad-band array, *Geophys. Res. Lett.,* **11,** 620–623.

Zhao, D. & Lei, J., 2004. Seismic ray path variations in a 3D global velocity model, *Phys. Earth planet. Inter.,* **141,** 153–166.

Zhu, A.N. & Wysession, M.E., 1997. Mapping global D″ P velocities from ISC PcP-P differential travel times, *Phys. Earth planet. Inter.,* **99,** 69–82.

Zhu, L.P. & Kanamori, H., 2000. Moho depth variation in southern California from teleseismic receiver functions, *J. Geophys. Res.-Solid Earth,* **105,** 2969–2980.

SUPPLEMENTARY MATERIAL

The following supplementary material is available for this article:

Appendix S1. The Appendix provides a series of supplementary figures for this article. Figure. A. Shows transverse component velocity synthetics. Figure B. Transverse component displacement synthetics. Figure C. Lower-mantle cross-sections for (a) 1-D D″ discontinuity models of Lay *et al.* (2004b), (b) model LAYB and (c) model THOM2.0. Figure D. Lower-mantle cross-sections for model TXBW. Figure E. Whole mantle cross-sections for model TXBW. Figure F. Comparison of synthetics computed for the 1-D D″ models of Lay *et al.* (2004b) with synthetics created for model LAYB. Figure G. Comparison of synthetics computed for models THOM1.5 and THOM2.0. Figure H. Example record sections at seismic stations PAS (a) and GSC (b). Figure I. Differential traveltimes.

This material is available as part of the online article from: http://www.blackwell-synergy.com/doi/abs/10.1111/j.1365-246X.2006.03279.x (This link will take you to the article abstract).

Please note: Blackwell Publishing are not responsible for the content or functionality of any supplementary materials supplied by the authors. Any queries (other than missing material) should be directed to the corresponding author for the article.